Seismicity and shallow slab geometry in the central Vanuatu subduction zone

Christian Baillard, W. C. Crawford, V. Ballu, M. Regnier, B. Pelletier, E. Garaebiti

To cite this version:

Christian Baillard, W. C. Crawford, V. Ballu, M. Regnier, B. Pelletier, et al.. Seismicity and shallow slab geometry in the central Vanuatu subduction zone. Journal of Geophysical Research : Solid Earth, 2015, 120 (8), pp.5606-5623. 10.1002/2014JB011853 . hal-01256424

AGU PUBLICATIONS

JGR

Journal of Geophysical Research: Solid Earth

RESEARCH ARTICLE

10.1002/2014JB011853

Key Points:
- Shallow bulge of the subduction interface in front of the seamount
- The upper mantle wedge is not significantly serpentinized
- The maximum width of the seismogenic zone is 80 km (~7.6 M_w earthquake)

Supporting Information:
- Texts S1–S3, Figures S1–S6, and Tables S1 and S2

Correspondence to:
C. Baillard,
baillard@ipgp.fr

Citation:
Baillard, C., W. C. Crawford, V. Ballu, M. Régnier, B. Pelletier, and E. Garaebiti (2015), Seismicity and shallow slab geometry in the central Vanuatu subduction zone, *J. Geophys. Res. Solid Earth*, *120*, 5606–5623, doi:10.1002/2014JB011853.

Received 19 DEC 2014
Accepted 1 JUL 2015
Accepted article online 14 JUL 2015
Published online 13 AUG 2015

Seismicity and shallow slab geometry in the central Vanuatu subduction zone

Christian Baillard[1], Wayne C. Crawford[1], Valérie Ballu[2], Marc Régnier[3], Bernard Pelletier[4], and Esline Garaebiti[5]

[1]Institut de Physique du Globe de Paris, Université Paris Diderot–PRES Sorbonne Paris Cité, Paris, France, [2]Littoral Environnement et Sociétés, Université de La Rochelle, La Rochelle, France, [3]Géoazur, Université Nice Sophia-Antipolis, Valbonne, France, [4]Institut pour la Recherche et le Développement, Nouméa, New Caledonia, [5]Vanuatu Meteorology and Geohazards Department, Port Vila, Vanuatu

Abstract The Vanuatu arc in the southwest Pacific Ocean is one of the world's most seismically active regions, with almost 39 magnitude 7+ earthquakes in the past 43 years. Convergence rates are around 90–120 mm/yr along most of the arc, but drop to 25–43 mm/yr in the central section, probably due to the subduction of the d'Entrecasteaux ridge. We characterize the slab geometry and tectonic state in this central section by analyzing data from a 10 month deployment of 30 seismometers over this section. We located more than 30,000 events (all less than magnitude 5.5), constructed an improved 1-D velocity model, calculated focal mechanisms and cluster geometries, and determined the 3-D geometry of the interplate seismogenic zone. The seismogenic zone has a shallow bulge in front of the d'Entrecasteaux ridge, which could be explained by the ridge's buoyancy contributing to the uplift of the fore-arc islands. The seismogenic zone extends to ~45 km depth, significantly below the 26–27 km depth of the fore-arc Moho, indicating that the upper mantle wedge is not significantly serpentinized, which is consistent with the relatively high thermal parameter of the subducting plate. The maximum width of the seismogenic zone is 80 km, indicating an upper earthquake magnitude limit of M_w 7.85 ± 0.4, assuming standard rupture zone aspect ratios. The data also reveal a double seismic zone, 20 to 30 km below the seismogenic zone, which is presumably caused by flexure of the downgoing plate.

1. Introduction

Subduction zones create some of the Earth's most important geohazards, including megathrust earthquakes, tsunamis, and intense volcanic eruptions. Despite great efforts by the scientific community to understand subduction zones, many questions remain unanswered, including What parameters control the occurrence of megathrust earthquakes and the propagation of ruptures during these earthquakes? What is the role of the topography of the subducting plate (i.e., the presence of seamounts or the existence of fracture zones) in the generation and propagation of mega-earthquakes? How far does the seismogenic zone extends and is its downdip limit controlled by the crust-mantle contact on the subduction interface or by thermal conditions?

The Vanuatu subduction zone (12–22°S, 166–171°E) is among the world's most seismically active subduction zones, with approximately 22 M_w 5.5+ earthquakes per year in the National Earthquake Information Center (NEIC) catalog (only the Tonga trench and Japan have similar rates over as long a stretch of plate boundary [*Heuret et al.*, 2011]). This intense activity is probably caused by the high convergence rate between the Australian Plate and the New Hebrides Plate across the subduction zone [*Ide*, 2013], which varies from 90 mm/yr (oriented 83° CW of N) at 13°S to 125 mm/yr (oriented 80° CW of N) at 22.5°S, according to the MORVEL model and assuming a fixed New Hebrides Plate [*DeMets et al.*, 2010]. There is, however, no evidence of great megathrust earthquakes ($M_w \geq 8.5$) in this zone, an observation shared with several intraoceanic subduction zones, such as Tonga and the Lesser Antilles [*Heuret et al.*, 2011]. This lack of great earthquakes correlates with a low seismic coupling coefficient (0.14, compared to a mean of 0.26 over all subduction zones [*Heuret et al.*, 2011]), defined as the ratio between the observed seismic slip rate and the globally calculated convergence rate.

The central section of the Vanuatu arc (15°S–17°S) is a remarkable area for studying subduction processes because there are large islands close to the subduction front. This section has the following singularities with respect to the rest of the arc: (1) the convergence rate across the trench, derived from local GPS studies, is

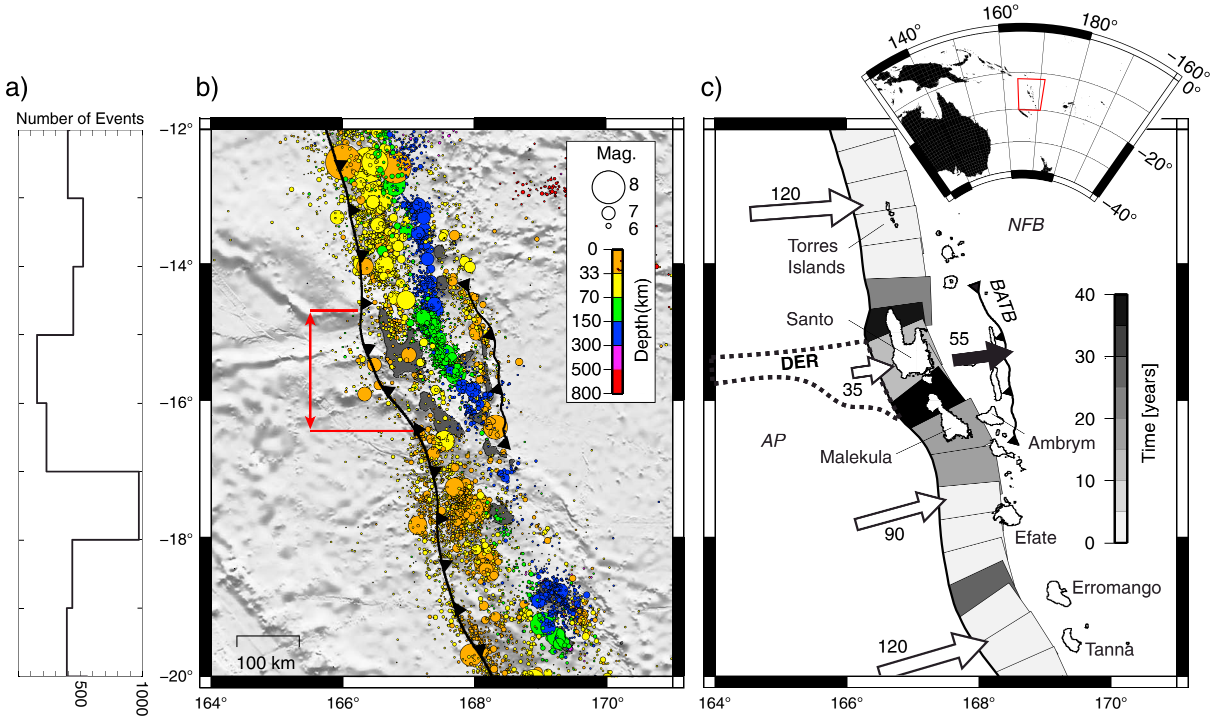

Figure 1. Seismic activity and geodynamics in the Vanuatu subduction zone. Seismicity data (M 4+) are from the 1973–2013 NEIC catalog. (a) Number of shallow events (depth <70 km) per 1° interval. (b) Earthquakes (depth indicated by color and magnitude by size). The red arrow indicates the extent of a seismic gap in the central section fore arc. (c) Time elapsed since the last $M_w > 6.5$ earthquake (depths <50 km). The white and black arrows represent, respectively, the convergence rates estimated at the trench and at the back-arc thrust belt, from local GPS data [*Calmant et al.*, 2003; *Bergeot et al.*, 2009]. AP: Australian Plate; DER: d'Entrecasteaux ridge; NFB: North Fiji Basin.

greatly slowed (25–43 mm/yr) [*Calmant et al.*, 2003; *Bergeot et al.*, 2009]; (2) globally detectable seismic activity is much lower, with a significant gap in maps of globally detected (M 4+) seismic activity (Figure 1) and an anomalously long time since the last $M_w > 6.5$ event (15 to 40 years, compared to less than 10 years for the rest of the arc); and (3) fore arc tectonic uplift is significant over the last 100 kyr, creating relief up to 1800 m above sea level with a maximum rate of 6 mm/yr measured on Santo Island [*Taylor et al.*, 2005].

These singularities are geographically correlated to the subduction of the d'Entrecasteaux ridge facing the large fore-arc islands of Santo and Malekula [*Taylor et al.*, 1980, 1995, 2005; *Pelletier et al.*, 1994]. The slowed convergence rate, currently accommodated by convergence within and behind the arc, may be a partially short-term effect due to interseismic locking of the subduction interface segment. To understand the current state of plate locking and stress, we deployed 30 wideband seismometers in a network covering the fore-arc islands and the ocean between them and the subduction front. The deployment was part of the 2008–2009 ARC-VANUATU geodynamic experiment, which also included GPS field campaigns (continuing time series started in 1996) and the installation of seven continuous GPS stations on the central Vanuatu Islands. This paper focuses primarily on the seismological experiment; we used more than 9500 earthquakes located beneath the network during the 10 month deployment to define the geometry of the subduction zone interface, determine the extent of the seismogenic zone, and evaluate the state of stress around the megathrust interface. Because the central part of the Vanuatu arc is characterized by the intraoceanic subduction of an underwater ridge, our study provides some constraints on the role of subducting asperities on the shape and coupling of the seismogenic zone. We also use our constraints on the size of the seismogenic zone to estimate the potential for a major ($M > 8$) earthquake.

2. ARC-VANUATU Seismic Data

The ARC-VANUATU seismological network consisted of 20 wideband seismometers covering the southern half of Santo Island and the northern part of Malekula Island and 10 wideband ocean bottom

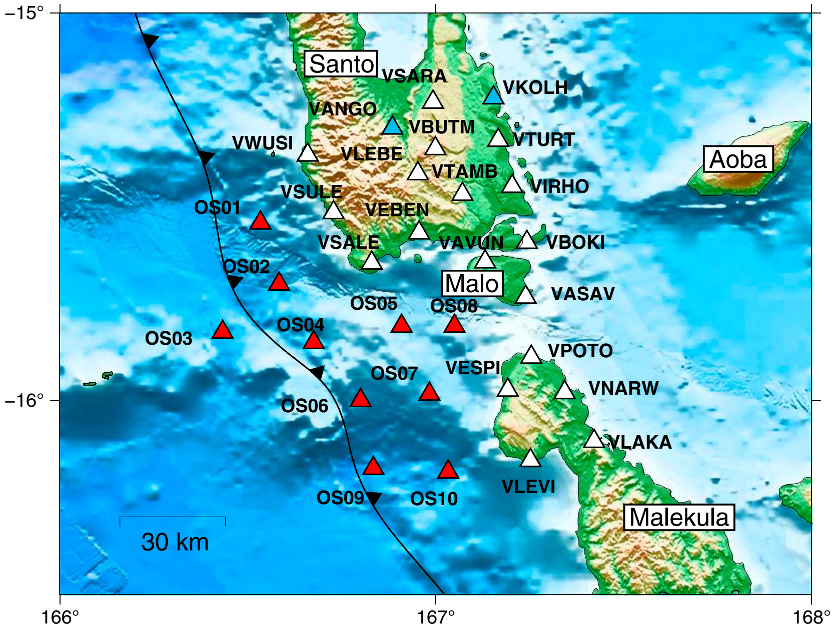

Figure 2. Map of the 2008–2009 ARC-VANUATU local seismological network, composed of 20 broadband land stations (white and blue triangles) and 10 OBSs (red triangles). The two blue triangles indicate the land stations with significant recording gaps. Island names are given in text on white background boxes and station names in text without background.

seismometers (OBSs) offshore (Figure 2). All of these instruments used Guralp CMG-40T seismometers, and the OBSs also used short-period hydrophones. The onshore data cover 10 months (from May 2008 to February 2009), and the OBS data cover four of these months (from the middle of May 2008 to August–September 2008). The aperture of the network was roughly 100 × 100 km, and the average distance between instruments was approximately 20 km.

Due to a manufacturing defect, only two of the OBSs functioned properly: for the other OBSs, we used the hydrophone channels. Land stations VANGO and VKOLH (blue triangles in Figure 2) had significant recording gaps: 4 and 7 months, respectively.

3. Methodology

3.1. Earthquake Automatic Picking

More than 40,000 earthquakes (approximately 1 every 10 min) were detected on five or more instruments using an STA/LTA algorithm [*Allen*, 1982]. Due to the large number of events, we decided to use an automatic picking procedure (APP). After unsatisfactory comparison of existing APPs with manual picks, we developed a new APP based on the kurtosis function and automatic phase identification [*Baillard et al.*, 2014; *Hibert et al.*, 2014]. We use this APP to automatically pick P and S wave onsets and to estimate the local magnitude of events. The time difference between the APP and a subset of 163 manually picked events was 0.01 ± 0.08 s for P waves and -0.09 ± 0.23 s for S waves, and the APP actually provided more locations than the manual picking [*Baillard et al.*, 2014]. Applied over the entire data set, the APP provided locations for approximately 30,000 of the 40,000 detected events, using a 1-D "starting model" from *Prevot et al.* [1991] and the HYPOCENTER earthquake location software [*Lienert and Havskov*, 1995]. These locations constitute our "preliminary catalog." M_L in this catalog ranges from −0.5 to 5.4, and 95% of the events have $M_L < 3.1$.

3.2. Velocity Model

We next calculated an improved 1-D model to locate the earthquakes, using a high-quality subset of 285 hypocenters from our preliminary catalog that (1) were picked on at least 10 stations, (2) were located beneath the network (GAP < 180°), (3) had a residual < 0.5 s, and (4) had location errors < 10 km. The 285

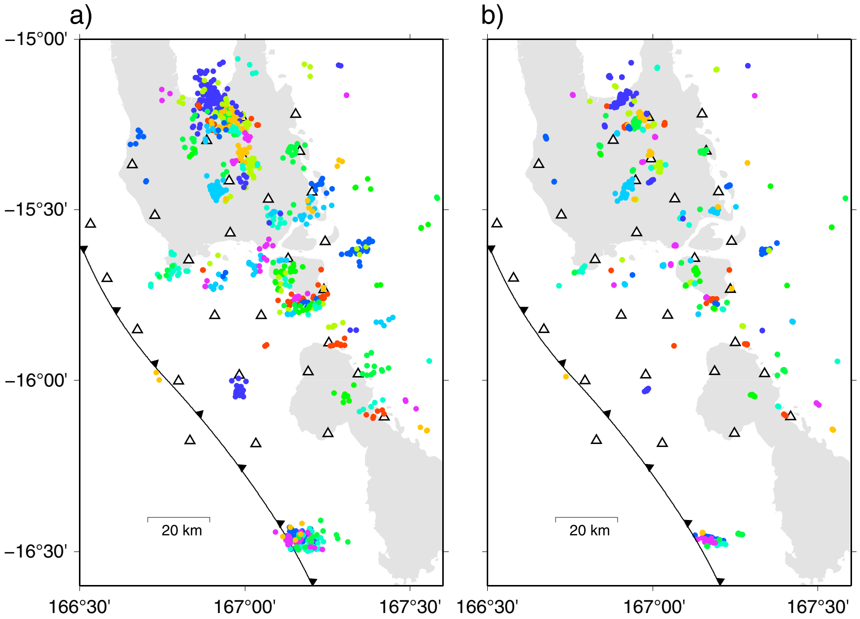

Figure 3. Results of double difference event relocation. Events are shown by circles, and events in the same cluster have the same color. In both panels, only events not dismissed during the relocation process are shown (the same events are shown in both panels). The white triangles represent the seismological stations. (a) Earthquakes before relocation. (b) Earthquakes after relocation.

selected hypocenters have 3695 *P* picks and 2845 *S* picks, depths between 7 and 50 km, and the same average M_L as the preliminary catalog.

We calculated the improved 1-D model using a Monte Carlo approach to define the best (V_p, V_s) model. We assumed a constant V_p gradient from 0 to 50 km depth and a constant V_p/V_s ratio throughout the model. We tested 400 models covering the physically feasible range of vertical V_p gradients, V_p/V_s ratios, and topmost layer velocities. We imposed a positive V_p gradient with depth after confirming that negative gradients did not improve the final residuals and increased instability. As we had no earthquakes below 50 km in the high-quality subset, we imposed the average International Association of Seismology and Physics of the Earth's Interior gradient for depths below 50 km [*Kennett and Engdahl*, 1991]. The final (V_p, V_s) model has a residual of 0.243 s. We present and interpret the 1-D model in section 4.1.

HYPOCENTER also calculates station corrections: constant time shifts to be applied to each pick at each station in order to minimize the hypocenter residuals. These station corrections indicate and account for local, shallow variations in the velocity structure with respect to the 1-D model. Positive and negative station corrections are associated, respectively, with slower and faster local shallow velocities. We present and interpret station corrections in section 4.1.

We calculated the stability of our 1-D model using the procedure of *Husen et al.* [1999] (see Text S1 in the supporting information). The initial position of hypocenters does not significantly affect final hypocenter positions (Figure S1 in the supporting information), indicating that our 1-D velocity model provides stable results.

The final 1-D model provided 31,019 locations, which we refer to as the "total catalog." Sixty-eight percent of the earthquakes in our total catalog have residuals <0.5 s, compared to only 62% with the preliminary velocity model.

Spatial errors are important for events outside of the network (see "bootstrap" method in Text S2), so we also created a "local catalog" of events located under or very near to the network (inside a box from 166–167.75°E longitude, 15°S–16°S latitude, and 0–100 km depth). This catalog contains 9514 events, with M_L ranging from -0.5 to 4.5 (95% of the events have $M_L < 2.5$). The median depth error in this catalog is 11 km.

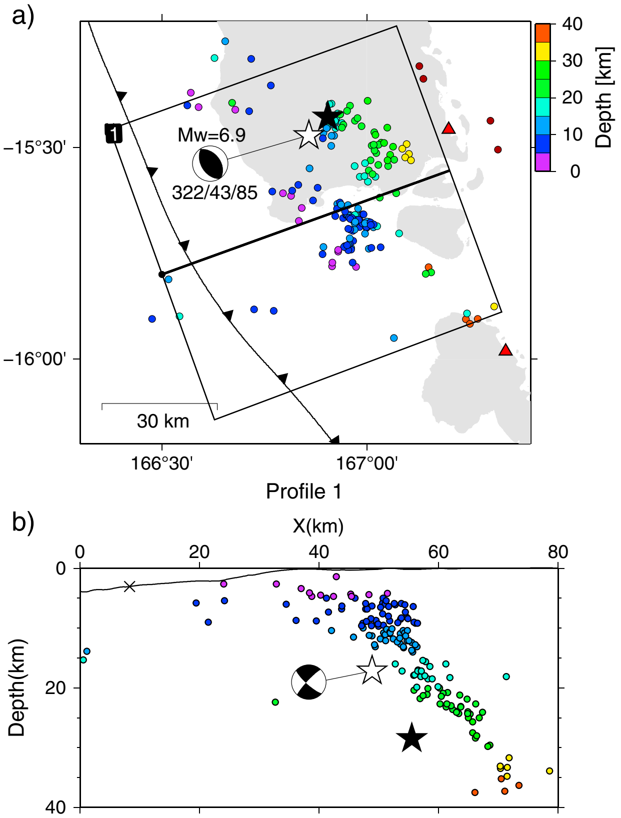

Figure 4. The 4 October 2000 M_w 6.9 earthquake and aftershock sequence. The black and white stars indicate the main shock located using global and local networks, respectively. Focal mechanism was calculated by waveform inversion [*Nabelek*, 1984]. The circles indicate the aftershocks located by the local network up to 10 days after the main shock: location errors range from 5 to 8 km. (a) Map view. The red triangles indicate some of the stations of the local network (the others are on islands further east). The focal mechanism strike/dip/rake is indicated under the beach ball. The box indicates the bounds and orientation of the profile shown in the cross section. (b). Cross section projected along profile 1. "X" indicates the subduction front.

3.3. Event Relocation

To investigate patterns of seismicity between nearby events, we calculated a "relocated" local catalog using the double-difference method [*Waldhauser*, 2000, 2001; *Waldhauser and Ellsworth*, 2002]. This method can greatly improve the relative locations of earthquakes that are near to one another and which have similar waveforms.

The primary input to the relocation method is the travel time delay between two similar events. The similarity of these events is defined by the similarity in waveforms, moveouts (arrival time delays at each station), and locations, indicating a common rupture mechanism and trajectory through the Earth. The time delay between a pair of similar events (obtained by computing the time offset of the cross correlation between two event waveforms at the same station) is directly linked to the distance separating their hypocenters.

We invert this "double difference" to improve the relative locations of similar hypocenters (see *Waldhauser* [2001] and Text S3 for details). We relocated 837 events (divided into 118 clusters) from our local catalog. Relocated events have M_L between 0.4 and 3.8 (95% with $M_L < 2.8$).

After relocation the geometries of the clusters are much better defined (Figure 3). We assessed the relative spatial errors of this relocated local catalog using a derived bootstrap method (Text S3). For all of the 118 clusters, the relative spatial error is less than 240 m, which is approximately 12% of the average cluster dimension. This means that the general shapes of relocated clusters are significant and can be used to interpret tectonic context.

3.4. Focal Mechanisms and Cluster Orientations

We computed focal mechanisms where possible, in order to constrain rupture processes and fault orientations. We used the HASH code [*Hardebeck and Shearer*, 2002] and only *P* polarities (because *P-S* amplitude ratios can vary by a factor 2 to 7 for similar events if noise levels are significant [*Hardebeck*, 2003]).

We could only pick polarities and compute the focal mechanisms for 10 events, all of which had $M_L > 3$ (see Table S1 in the supporting information). However, we were also able to calculate "composite" focal mechanisms for several of the relocated clusters of smaller events, using the assumption that events in a single cluster have similar locations and focal mechanisms [*Hardebeck and Shearer*, 2002]. We manually picked 2104 *P* polarities from the relocated clusters, obtaining 13 "reliable" composite focal mechanisms according to the following criteria: polarity mispicks <15%, mechanism coverage (HASH parameter STDR) >0.45, and pole errors <40° (see Table S2). The mean M_L of the events in these clusters is 1.7, and the maximum M_L is 3. We interpret these focal mechanisms in section 4.2.

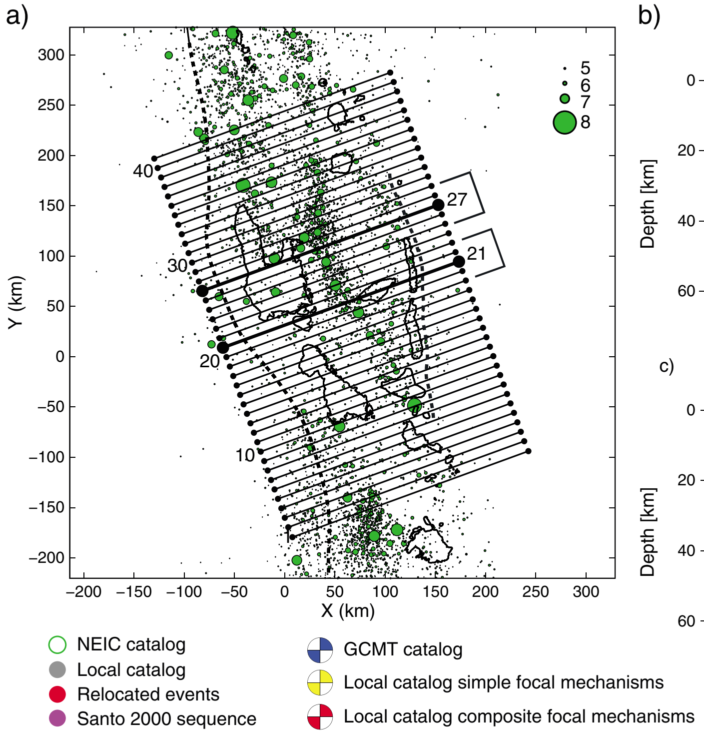

Figure 5. Overview of the method used to pick the subduction interface. (a) Map view showing the 41 N70°E oriented profiles used to pick the subduction plane. The numbered boxes to the east of the profiles show the across-profile range of hypocenters included when picking on a profile (for profiles 27 and 21, shown to the right). (b and c) Catalogs projected onto profiles 27 and 21, respectively. For clarity and to conserve the true geometry, we only show the first 140 km of the transects. The solid black line represents the manually picked subduction interface. The triangles indicate the local seismological network stations.

To characterize the type of seismic source associated with relocated clusters, we estimated the spatial orientation of clusters and compared with their composite focal mechanisms. We used a statistical approach called the three-point method to determine the clusters' spatial orientation [*Fehler et al.*, 1987; *Godano et al.*, 2014]. The method consists in determining the normal to the plane (or pole) defined by all possible combinations of three hypocenters belonging to the cluster. We calculate the statistical distribution of possible pole orientations for each cluster by repeatedly (~100 times) calculating the pole, each time randomly shifting the hypocenter according to its uncertainty [*Baillard*, 2014]. We compare this result with the two nodal poles defined by our composite focal mechanisms. A conceptual model of cluster orientation and pole comparison is shown in Figure S3, and two examples are presented in Figure S4.

Some clusters do not have a single preferred pole, for example a linear alignment of hypocenters for which the pole orientations are distributed in a circle orthogonal to the lineation. Before interpreting the pole orientation, therefore, we quantify the cluster shapes by calculating the three eigenvalues characterizing the ellipsoid ($\lambda_1 > \lambda_2 > \lambda_3$) surrounding the hypocenter cloud using a singular value decomposition [*Asanuma et al.*, 2001]. The shapes are divided into three classes based on the eigenvalues: lines ($\lambda_1 \gg \lambda_2$), planes ($\lambda_1 \approx \lambda_2$ and $\lambda_2 \gg \lambda_3$), and ellipsoids ($\lambda_1 \approx \lambda_2 \approx \lambda_3$). Results and interpretation of this classification and the orientations of the 13 clusters are presented in section 4.2.

3.5. Subduction Interface Geometry

To determine the geometry of the subduction plane beneath the central Vanuatu Arc, we combined our local catalog, including relocated events and focal mechanisms, with our total catalog, the NEIC catalog, the Harvard global centroid moment tensor catalog, and data collected by one of the authors during and after the M_w 6.9 Santo earthquake (4 October 2000) using a four-seismometer local network. The aftershock sequence of the Santo earthquake is particularly useful to define the subduction interface as there was no important megathrust earthquake during our experiment. The main shock of the 2000 Santo earthquake was located at 17 km depth, and the aftershock depths range from 5 to 40 km (Figure 4). In this paper, we

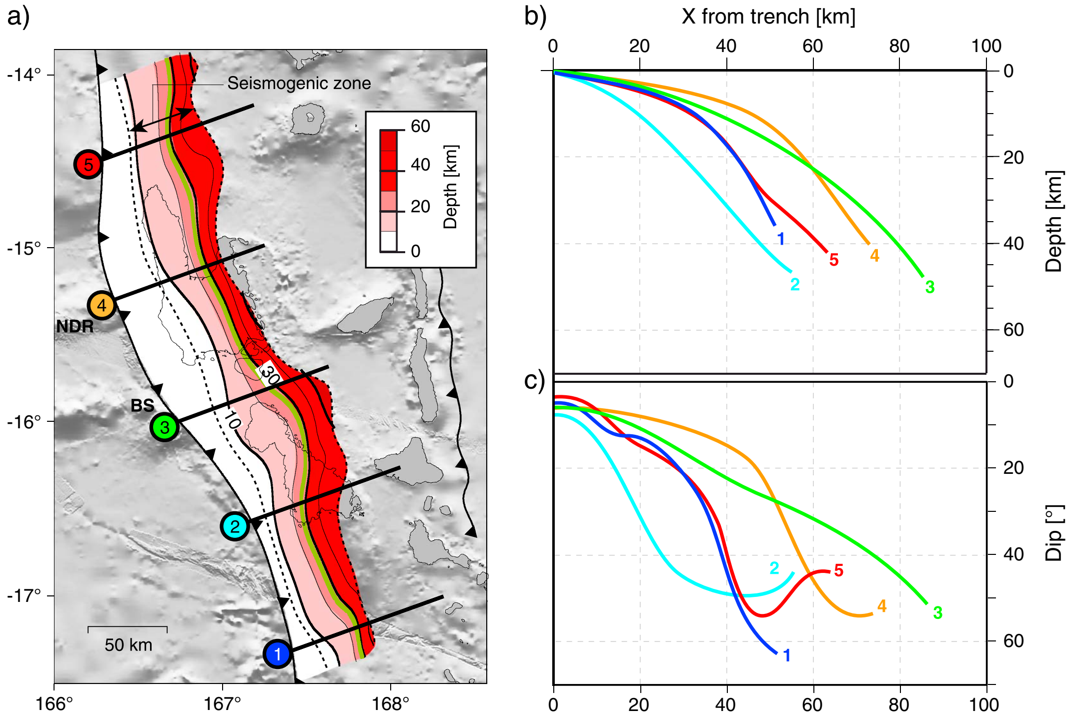

Figure 6. Geometry of the subduction interface and updip/downdip extents of the seismogenic zone. (a) Map view. The green contour is at 27 km depth and marks the intersection with the fore-arc Moho. The dashed contours present the updip and downdip extents of the seismogenic zone. The numbered lines show the location of cross sections plotted to the right. NDR: north d'Entrecasteaux ridge; BS: Bougainville seamount. (b) Geometric cross sections of the subduction interface (depth as a function of distance from the subduction front). (c) Dip cross sections (dip angle as a function of distance from the subduction front).

focus on the shallow part (<75 km depth) of the subduction interface, where location uncertainties are small in the local catalog (see Text S2 and Figure S2).

Automatic procedures exist to estimate the position of the subduction interface, but they require a significant density of large earthquakes with thrust mechanisms, which are assumed to lie on the subduction interface (e.g., the SLAB1.0 project [*Hayes and Wald*, 2009; *Hayes et al.*, 2012]). Our microearthquake catalog has scattered (but accurate) locations and few focal mechanisms, preventing automatic selection of events and determination of the main interface. We therefore decided to manually pick the position of the shallow subduction interface.

We developed a graphical user interface (GUI) to manually pick the subduction interface. We defined a grid made of 41 250 km long profiles oriented N70°E and spaced 10 km apart (Figure 5a). The GUI projects events lying within 20 km of the profile onto each profile. This overlapping of data across neighboring profiles ensures the continuity of the picked subduction plane (Figures 5b and 5c). We used all of the abovementioned catalogs and picked the main subduction interface corresponding to both an alignment of earthquakes and the presence of thrust mechanisms. Once we finished picking on all transects, we pinned the interface to the subduction front at the trench and fit a smoothed 3-D surface to the picked points.

The shallow seismogenic zone corresponds to the nonstable or conditionally stable portion of the subduction interface [e.g., *Scholz*, 2002]. We observed a strong reduction of seismic activity below 45 km depth (Figure 5), both on local and global catalogs, which we consider to correspond to the downdip limit of this seismogenic zone. Figure 6 shows the geometry of the subduction interface and the downdip extent of its seismogenic zone. We discuss these observations in sections 4.3 and 4.4.

4. Results and Discussion

4.1. Velocity Model Interpretation

Figure 7 shows the final (V_p, V_s) 1-D model obtained for the Santo and Malekula region. We emphasize that this is a local model derived from events underneath the network and may not apply outside of the

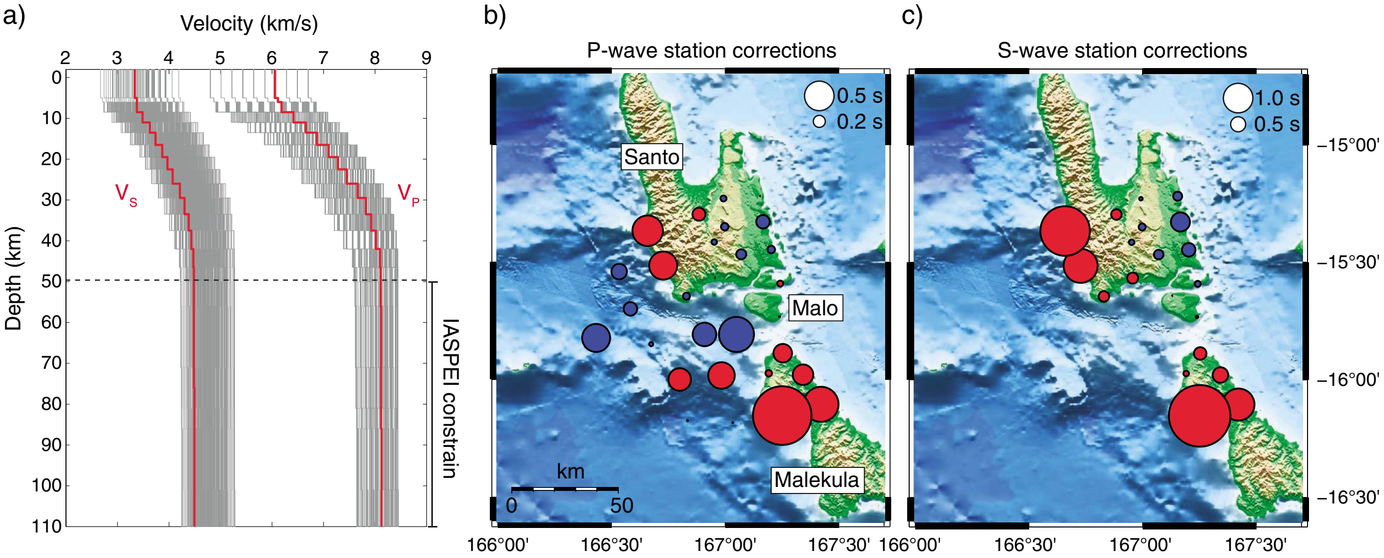

Figure 7. One-dimensional velocity model and station corrections. (a) Tested (gray) and final (red) (V_p, V_s) models. (b and c) Station corrections for *P* and *S* waves, respectively. Positive corrections are represented in red and negative in blue. Positive corrections indicate slower local shallow velocities than in the 1-D model. The scale of the circles is different for the two maps.

network. The top layer velocity is 6 km/s, the velocity gradient is ~0.04 km/s/km over the first 50 km, and the V_p/V_s ratio is 1.8 (Figure 7). The *P* velocity of 6 km/s for the first 7 km gives a similar average velocity over the first 15 km to the value of 6.6 km/s estimated for the first 15 km by *Prevot et al.* [1991]. The V_p/V_s ratio of 1.8 is close to the ratio of 1.78 indicated from the Wadati diagram computed using our *P* and *S* pick arrival times. Station corrections for *P* waves show the same pattern as those for *S* waves, but the *S* wave station corrections are approximately twice the *P* wave station corrections, consistent with the V_p/V_s ratio of 1.8 (Figure 7). Our model reaches a velocity of 7.6 km/s at 26 km depth, which corresponds well to *Coudert et al.*'s [1984] estimation of a fore-arc Moho depth of 27 ± 4 km with a *P* velocity of 7.6 km/s. This relatively thick fore-arc crust is probably related to the strong compressive stress endured by the fore arc due to the subduction of the bathymetric highs.

Station corrections (Figure 7) indicate low-velocity anomalies on the western part of Santo and the north of Malekula, which are probably the result of altered and fractured rocks in the western mountain chain, resulting from E-W compression [*Meffre and Crawford*, 2001]. The higher shallow velocities beneath eastern part of Santo are consistent with compacted limestones (experimental measures on analogous limestones show a velocity of 4.5 km/s to 6.5 km/s [*Castagna et al.*, 1985]) due to the underwater history of Santo in the late Miocene [*Pelletier et al.*, 1994].

The strong shallow velocity heterogeneity indicates the complexity of Earth's structure, partly due to the asymmetrical geological context inherent to subduction zones. We see here the limits of the 1-D model, which is sufficient to reduce hypocenter location errors but inadequate to fully interpret the 3-D velocity structure. A 3-D tomographic model should be calculated in the future using our local catalog.

Nevertheless, the improved 1-D velocity model provides a well-constrained microearthquake catalog. Projecting these earthquakes on a profile orthogonal to the trench provides a good overview of the seismic activity on and around the subduction plane (Figure 8) and reveals three regions of dense seismic activity: (1) shallow earthquakes on or near the subduction interface, which we call interplate earthquakes; (2) shallow earthquakes in the downgoing plate below the subduction interface, which we call shallow intraplate earthquakes; and (3) intermediate-depth earthquakes that are most likely located in the downgoing plate. We will focus on the first two sets of earthquakes, which are the best located by our network.

4.2. Geometry of Clusters and Relation With Composite Focal Mechanisms

The earthquakes present a great variety of focal mechanisms (Figure 9). Most of the simple thrust fault mechanisms in our catalog are situated at 20 to 35 km depth beneath Malo Island. Two of the 13

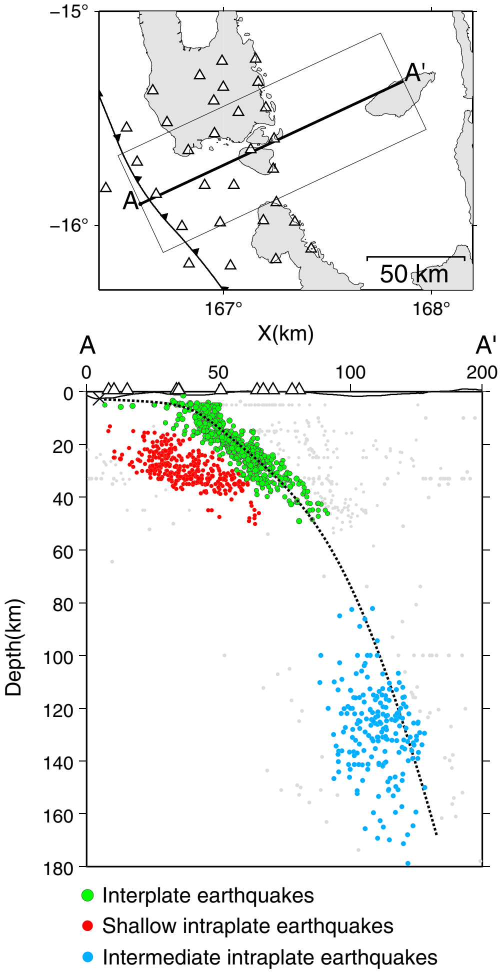

Figure 8. Cross section of seismic activity through the center of our total catalog (only events with residuals <0.2 s are plotted). Three clusters of activity are observed: (1) around the subduction interface (green), (2) within the subducting plate beneath the subduction interface (red), and (3) at intermediate depths (blue). The dotted line is our interpretation of the subduction interface.

composite focal mechanisms (clusters 1 and 5), both beneath north Santo, have clear thrust mechanisms, and a third (cluster 15), beneath Malo, has a thrust-dominated mechanism. The depths of all of these events correspond well to the subduction interface indicated by the combined catalogs and provide local constraints on the position of this interface.

The remaining composite focal mechanisms are highly heterogeneous, indicating a complex state of stress. There are no preferential axes of compression: for example, clusters 12 and 14 present orthogonal compressive axes even though they are located only ~20 km apart.

Can these composite focal mechanisms be related to the cluster shapes? A plane shape could be caused by an activated patch of fault surface, whereas a line-shaped cluster could be caused by a ridge on the plate interface, a channel or crack along a fault, or a series of en echelon cracks. Two of the clusters have a planar shape, eight have linear shapes, and three have ellipsoidal shapes (Figure 10a). An elliptical shape provides no geometric information, and so we do not interpret these latter three clusters here.

The simplest case to interpret is where the cluster geometry aligns with one of the nodal planes, in which case we can consider that the cluster sits on the rupture plane. Only four clusters (1, 6, 7, and 8) have this characteristic (see Figure S4 for two examples). Clusters 1, 6, and 8 lie on or very close to the subduction interface, but each has a different behavior/context. Cluster 1 has a linear shape and a thrust mechanism aligned with the megathrust interface: we interpret it as a linear asperity, possibly a ridge, on the megathrust interface (Figure 10b). Cluster 6 has a linear shape, a normal mechanism, and appears to lie slightly beneath the subduction interface: we interpret it as events on a normal fault within the subducting plate, possibly activated by bending-induced extension (Figure 10c). Finally, cluster 8 has a planar shape, a strike-slip mechanism, and appears to lie above the subduction interface: we interpret this cluster as events along a strike-slip fault in the overriding plate between Santo and Malekula Islands (Figure 10d). This region is interpreted as a tectonic discontinuity based on reefal terraces and seismicity [*Taylor et al.*, 1980; *Ebel*, 1980]; cluster 8 could lie on a fault that is part of this discontinuity. The focal plane of this cluster is subparallel to the arc-perpendicular discontinuity, suggesting that the adjustment may occur along several subfaults.

Interpretation of the remaining nonellipsoidal clusters, whose poles are not aligned with a focal plane, is more speculative. Line-shaped clusters 17 and 18 have a nodal pole that aligns with one of the focal mechanism nodal plane poles, suggesting that the cluster could be a localized response to the stress field. The possible poles of line-shaped clusters 11, 13, and 14 are neither aligned with their focal planes nor with their nodal plane poles.

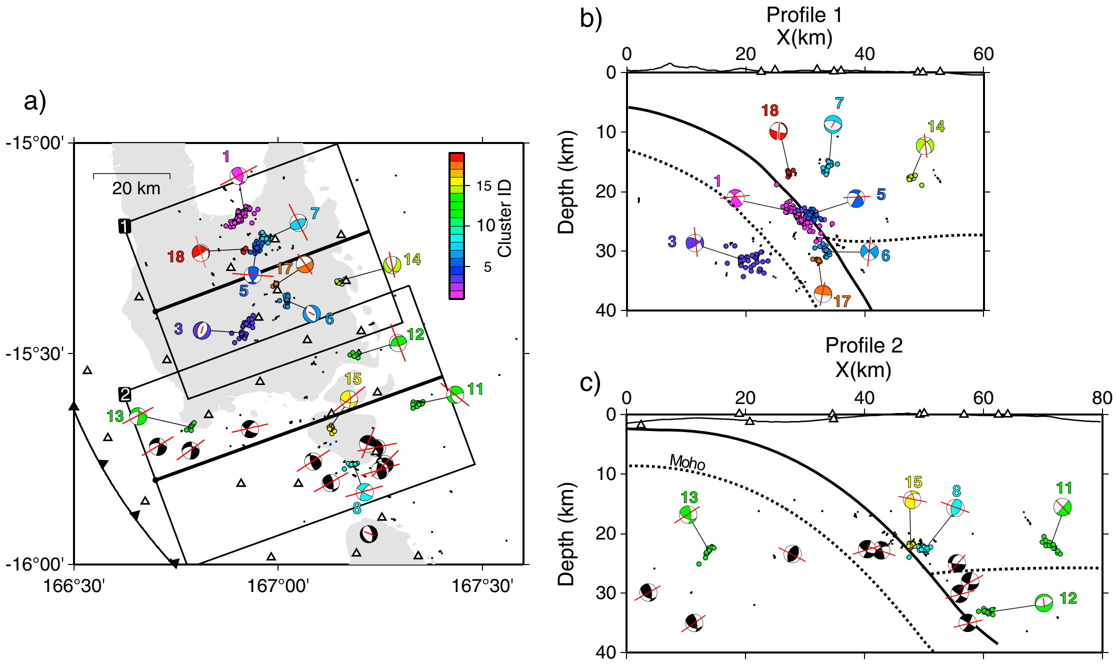

Figure 9. Clusters and focal mechanisms in the local catalog. Simple focal mechanisms are illustrated in black, composite focal mechanisms in colors corresponding to the cluster events (circles). *P* axes indicated in red. (a) Map view. The boxes indicate the orientation and dimensions of the cross sections. (b) Cross section beneath Santo Island. (c) Cross section between Santo and Malekula Islands. The cross sections also show the picked subduction interface (thick black curve), the Australian Plate Moho (dotted line, assuming a 8 km thick crust), and the North Fiji Basin Moho (dotted line, assuming a 27 km thick fore-arc crust).

This is possible in the case of coalescence and propagation of fractures along multiple preexisting flaws which are not aligned with the current stress direction [*Brace and Bombolakis*, 1963; *Bobet and Einstein*, 1998], which would tend to create "en échelon" ruptures along the main compression axis.

The relation between the cluster shape poles and their focal mechanisms appears to be highly dependent on the distance from the subduction interface: very near to the interface (clusters 1, 6, and 8), the shapes are aligned with a focal plane; farther away (clusters 17 and 18), they are aligned with a nodal plane pole; and even farther away (clusters 11, 13, and 14), they are aligned with neither (Figure 9). This relationship suggests an increasingly chaotic fault/rupture structure (and stress field) with increasing distance from the subduction interface.

Seismic activity does not migrate spatially over time within the clusters (Figure S5), and there is no clear evidence for repeated events within the relatively short (10 month) period of the experiment. Waveform correlations within clusters average 0.82 and are almost always less than the threshold of 0.95 commonly associated with repeated events [e.g., *Igarashi et al.*, 2003].

4.3. Influence of Subducted Topography on the Subduction Interface Geometry

The subduction interface generally has a shallow dip (<15°) over the first 20–40 km from the trench then rapidly bends, reaching approximately 40° dip at 40 km depth (Figure 6). The shallow-dipping zone extends farthest from the trench (40–50 km) in front of the region where the Bougainville and north d'Entrecasteaux seamounts subduct (Profiles 3 and 4). This bulge covers approximately 100 km along axis, from north Malekula to central Santo. The interface is generally shallower than that in the Slab 1.0 model [*Hayes et al.*, 2012], particularly within 50 km of the subduction front. In the region of the bulge, the interface is up to 30 km shallower than the Slab 1.0 model.

The bulge is probably created by the continuation of the ridge system associated with the Bougainville and d'Entrecasteaux seamounts. A positive density anomaly associated with these ridges would buoyantly resist subduction into the asthenosphere [*Wai-Ying and Kanamori*, 1978; *Cloos*, 1993], pushing the plate interface upward and reducing its dip [*Gerya et al.*, 2009]. This effect might also explain the up to 6 mm/yr uplift of south Santo over the past 110 kyr [*Taylor et al.*, 2005]. Simple mechanical models of

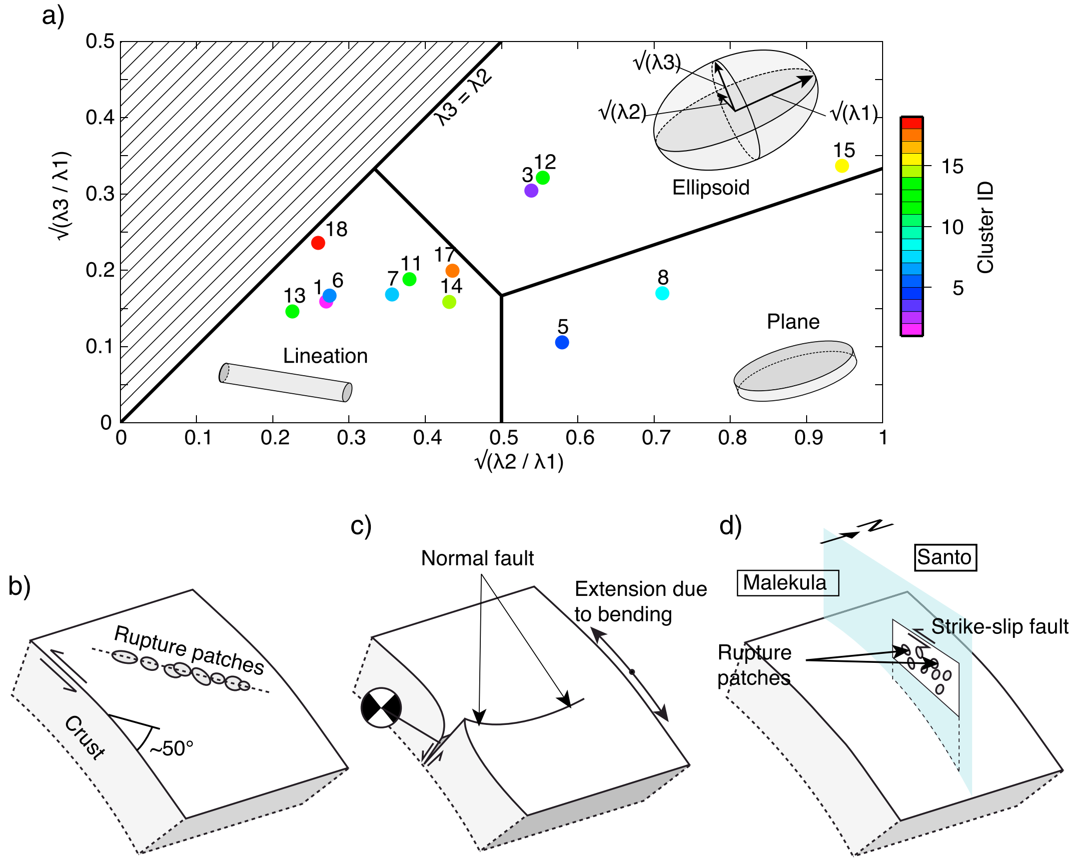

Figure 10. Cluster geometries and rupture models. (a) Classification of earthquake clusters depending on cluster shape eigenvalues. (b) Conceptual model for cluster 1 (line shape, thrust mechanism, localized on the subduction interface). (c) Conceptual model for cluster 6 (line shape, normal fault mechanism, just beneath the subduction interface). (d) Conceptual model for cluster 8 (vertical planar shape, strike-slip mechanism orthogonal to the trench and above the subduction interface).

buoyant ridges in other regions suggest uplifts of 3.7 mm/yr (the Cocos Ridge beneath Costa Rica [*Gardner et al.*, 1992]) and 0.9 mm/yr (the Hikurangi Plateau beneath New Zealand [*Litchfield et al.*, 2007]), smaller than but (in the case of the Cocos Ridge) on the order of the maximum central Vanuatu uplift. Additional uplift could be caused by geometrical surrection due to the impingement of the bathymetric highs [*Taylor et al.*, 2005] and nonelastic deformation, as suggested by the dense E-W compressional fault network in the high mountain ridge of west Santo [*Meffre and Crawford*, 2001].

Additional uplift could also be created by the readjustment of asthenosphere fluid flow above a sinking detached slab. *Chatelain et al.* [1992] proposed that the slab is detached beneath Malekula based on two principal observations: (1) the existence of a 150 km wide seismic gap beneath Malekula that extends south to Efate Island and (2) the severe attenuation and low average velocity of seismic waves passing through this gap [*Marthelot et al.*, 1985; *Prevot et al.*, 1991]. *Chatelain et al.* [1992] calculated that such a detachment could generate uplift rates of 0.3 to 3 mm/yr. However, the International Seismological Centre seismic catalog (data since 1910) reveals a less clear seismic gap with a maximum downdip width of 80 to 100 km, and seismic gaps are not necessarily associated with absence of a slab [e.g., *Hyndman et al.*, 1997; *Scholz*, 1998]. In this case, the low observed seismic wave velocities could be associated with hydrated blueschists [*Abers*, 2000] and the wave attenuation with the dehydration of these facies with depth [e.g., *Takemura and Yoshimoto*, 2014]. We do not deny the possibility of a detached slab, but a continuum slab is also possible and coherent with more recent data and interpretations made in other subduction zones.

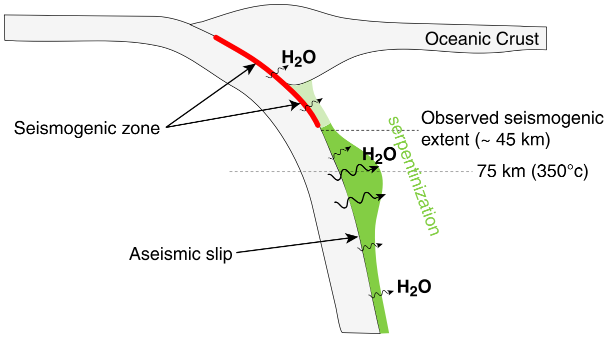

Figure 11. Conceptual model of why the downdip limit of the seismogenic zone extends to ~45 km. The subducting plate is relatively cold (high thermal parameter), and dehydration does not peak until ~75 km beneath the seafloor [*Maruyama and Okamoto*, 2007], leading to weak serpentinization of the upper mantle wedge. The downdip limit marks the depth at which the mantle is sufficiently serpentinized to allow stable sliding.

4.4. Characterization of the Seismogenic Zone

The seismogenic zone is defined as the nonstable portion of the subduction interface that allows nucleation of thrust earthquakes [e.g., *Scholz*, 1998]. Half of the seismic activity and seismic moment released in our local catalog is located on this zone, mostly concentrated around 25 km depth.

We estimate the updip limit of this zone to be 10 to 30 km from the subduction front (Figure 6a), based on the limit of aftershocks following the 2000 Santo earthquake. Our local catalog does not detect much seismic activity less than 30 km from the subduction front, but this could be due to the lesser sensitivity of our network near the subduction front (the OBSs were only deployed for 40% of the network time, and they had lower sensitivity than the land stations) or to blockage of the seismogenic zone closer to the subduction front during our experiment [e.g., *Bergeot et al.*, 2009].

The downdip limit varies between 35 and 50 km depth, with a mean depth of ~45 km (Figure 6). The subducted bathymetric highs associated with the bulge in the subduction interface are not associated with any change in this depth, indicating that the nonstable behavior of the seismogenic zone is not significantly influenced by the rheology or structure of the subducted seamounts. This limit is well below the ~27 km depth of the crust/mantle interface in the overriding plate, contradicting the assumption [e.g., *Tichelaar and Ruff*, 1993; *Hyndman et al.*, 1997] that the downdip limit for intraoceanic subduction is at the crust/mantle interface because serpentinization of the mantle wedge creates a stable sliding condition. Our results agree with a more recent global study of subduction zones showing that the downdip limit extends 10 km deeper than the upper plate crust/mantle interface in 70% of the studied seismogenic zones [*Heuret et al.*, 2011]. That study focused mostly on ocean-continent subduction zones, but recent local studies of intraoceanic subduction zones support this observation: *Dessa et al.* [2009] showed that the 2004 Andaman-Sumatra earthquake (9 to 9.3 M_w) nucleated below the fore-arc Moho, and *Laigle et al.* [2013] revealed interplate seismicity below the crust-mantle interface in the Lesser Antilles subduction zone.

In the Vanuatu region, the deep penetration of the downdip limit may be explained to a first order by the high thermal parameter of the downgoing Australian Plate. The thermal parameter reflects the capacity of a plate to rapidly bring cold material into the mantle and is defined as $\Phi = A * V * sin(\delta)$, where A is the age of the downgoing plate, V is the convergence velocity, and δ is the dip of the subduction interface. In central Vanuatu, A is approximately 57 Ma [*Collot et al.*, 1985], V is 49 to 70 mm/yr over geologic timescales [*Taylor et al.*, 1995], and the mean shallow dip is ~30°, giving $\Phi = 1400–2000$. This range of values is generally higher than the global average of ~1500 over all subduction zones [*Heuret et al.*, 2011], indicating that the downgoing plate has a higher-than-average capacity for carrying cold material to the mantle. *Maruyama and Okamoto* [2007] determined that cold subducting crust may not substantially dehydrate until ~75 km depth. Without substantial crustal dehydration, the mantle wedge will only be weakly hydrated/serpentinized and the subduction interface will have a nonstable behavior [*Shimada et al.*, 1983]. The downdip limit of interface seismicity suggests that the mantle becomes hydrated enough to allow stable sliding at about 45 km depth (Figure 11).

4.5. Maximum Earthquake Limit and Recurrence Time

What are the constraints on the maximum earthquake size and minimum recurrence interval in the region of south Santo and north Malekula? There is no absolute answer, as great earthquakes have a tendency of breaking established hypotheses, but we can suggest bounds based on scale laws which link rupture parameters and magnitude of earthquakes. We will show below that our seismological data, existing geodetic data, and the rather short historical record converge on a maximum earthquake magnitude of ~7.6 M_w, with a recurrence interval of 50–180 years, depending on the coupling coefficient. We use the subduction zone earthquake scaling parameters of *Strasser et al.* [2010] to relate rupture size to magnitude. We assume a shear rigidity, μ, of 5×10^{11} dyn/cm^2 [*Heuret et al.*, 2011] to relate slip to the magnitude using the definition of moment magnitude, $M_w \equiv \frac{2}{3}\log(DA\mu) - 10.7$, where A is the rupture area and D is the average displacement over the surface. The biggest uncertainty is the interseismic convergence rate, which is 25 to 43 mm/yr according to a local geodetic network in place since 1996 [*Calmant et al.*, 2003; *Bergeot et al.*, 2009] and 97 to 103 mm/yr according to the MORVEL regional plate velocity model [*DeMets et al.*, 2010]. The difference is presumably because of partial blocking by the subducting ridges and seamounts, which is accommodated by compression within and behind the island arc [*Calmant et al.*, 2003]. We use the local rate (25–43 mm/yr), as at least the back-arc compression is long established enough to create clear geological features: a higher convergence rate would not affect our calculation of the maximum earthquake magnitude but could reduce the recurrence interval.

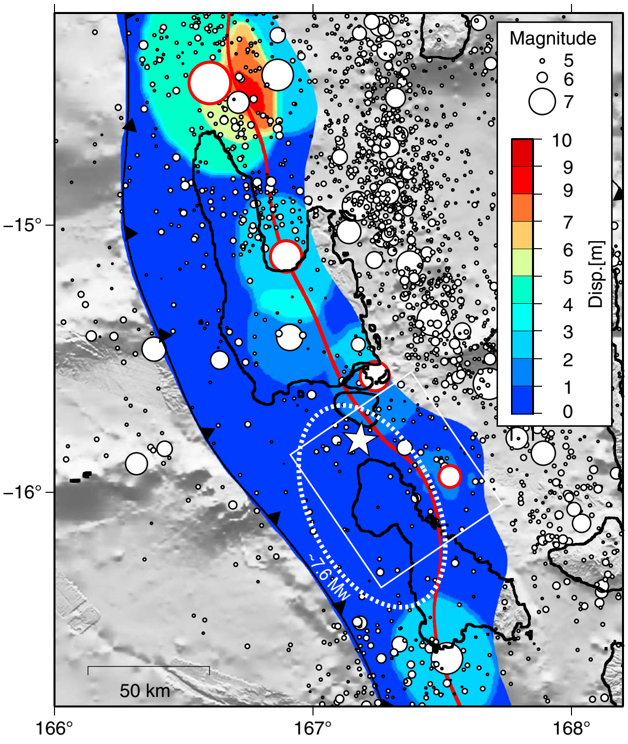

Figure 12. Map of modeled rupture patches associated with historical earthquakes (NEIC catalog 1973–2013, plus 1971 $M_S = 7.1$ and 1972 $M_S = 6.8$ earthquakes from *Chinn and Isacks* [1983]). Rupture patch size parameters are derived from *Strasser et al.* [2010]. The red circles represent the earthquakes whose provided magnitude is M_S rather than M_W. The main rupture gap since 1971 is indicated by the dotted ellipse. The white star and rectangle represent the, respectively, the epicenter and fault area model [*Ebel*, 1980] of the 1965 M_S 7.5 earthquake.

The dimensions of the locked zone are constrained by seismological data from our experiment and the 2000 Santo event aftershock measurements, as well as long-term geodetic data. The seismological data show a downdip limit 70–90 km from the trench along the interplate surface (Figure 6) and suggest an updip limit 10–30 km from the trench, giving a maximum rupture width of 60–80 km. (We here use the seismogenic width as the rupture width even though, in some cases, the earthquake rupture can overrun the seismogenic zone limits [*Scholz*, 2002].) *Bergeot et al.* [2009] estimated a locked zone width of 55 km (50 km horizontally with a 25° dip), using a simple back slip elastic model [*Savage*, 1983]. Using scaling laws for subduction earthquakes [*Strasser et al.*, 2010] a rupture width of 55 km corresponds to M_w 7.55 ± 0.4, whereas a rupture width of 80 km corresponds to M_w 7.85 ± 0.4. The upper magnitude limit in the central Vanuatu region is probably less than the latter value, as the blocked zone is unlikely to equal our maximum calculated value along the whole region and there appear to be barriers to earthquake propagation every 50–100 km along strike [*Ebel*, 1980; *Taylor et al.*, 1980]. In general, subduction zone earthquakes have a significantly greater rupture length than width, but one of the largest recorded earthquake in the region, the M_s 7.5 1965 event beneath south Santo and north Malekula, had a rupture length of only 70 km for a width of approximately 60 km [*Ebel*, 1980].

If we project rupture patches calculated from instrumentally constrained earthquakes (1971–2013, NEIC plus *Chinn and Isacks* [1983]) onto the subduction interface using the scaling relations of *Strasser et al.* [2010] (Figure 12), we observe a seismic gap from south Malo to mid-Malekula. This gap covers approximately the same region as the M_S 7.5 1965 event [*Ebel*, 1980]. The area of this gap is approximately 5000 km^2: filling it with one event would require a M_w 7.6 ± 0.3 earthquake [*Strasser et al.*, 2010]. The mean slip of such an earthquake would be from 0.6 m (for a M_w 7.3 event) to 3.2 m (for a M_w 7.9 event). The cumulated convergence in the 50 years since the 1965 event is 1.3–2.2 m, indicating that there is enough strain currently accumulated for a M_w 7.6–7.8 event if coupling is complete. The coupling coefficient of 0.14 calculated by *Heuret et al.* [2011] for Vanuatu, on the other hand, indicates a recurrence time of ~180 years for a M_w 7.6 event. However, the seismic coupling coefficient should be interpreted with caution, especially for earthquake recurrence intervals that are higher than the time range of recorded data. For example, the coupling coefficient in the Sumatra region was estimated to be 0.007 from 1900 to 1990 [*Pacheco et al.*, 1993], implying a small probability of a great megathrust earthquake. When the region was hit by the M_w 9.3 Andaman earthquake in 2004, the coupling coefficient increased to 0.98 [*Heuret et al.*, 2011]. Local geodetic (GPS and seafloor pressure/acoustic) data can help to quantify the actual current degree of locking on the subduction interface.

A high (~1) coupling coefficient and a faster long-term convergence rate than that measured locally by GPS could generate a recurrence interval of less than 50 years for a M_w 7.6 event, but geologic data indicate a lower limit of 50 years. *Taylor et al.* [1990] estimated a 50 year recurrence interval for the south Santo tectonic segment and a 422 year interval for north Malekula by fitting mean Holocene uplift rates to recent coseismic uplifts (considering earthquakes between M_w 7.1 and 7.9). Their calculation assumes that there is no interseismic vertical motion to compensate the coseismic motion, whereas local GPS measurements show clear interseismic vertical motions [e.g., *Bergeot et al.*, 2009; *Ballu et al.*, 2013]. Moreover, these interseismic motions are in the direction of the long-term uplift in south Santo and against the long-term uplift in north Malekula, which would tend to make the former recurrence interval estimate (50 years) too short and the latter (422 years) too long. However, this study has the advantage of covering a much larger time interval than the seismic data, and we therefore take 50 years as a lower limit of the seismic recurrence interval.

We showed above that the maximum width (80 km) of the seismogenic zone indicates an upper limit of M_w 7.85 ± 0.4 for earthquakes in the Santo-Malekula region. This is the upper limit of locked zone dimensions, and there are no historical (post-1900) earthquakes larger than M_s 7.5 in this region (there was one M_s 7.8 earthquake in 1910, but it appears to have been on the Australian Plate before subduction; Figure S6). Larger events (up to M_w 8.2) have been recorded further north and south along the archipelago (from 12 to 21°S), suggesting a wider seismogenic zone outside of the central zone: the largest events are 5 M_w or M_s 7.8–8.2 events around the Torres Islands to the north (1934, 1957, 1966, and two in 2009) and 4 M_w or M_s 7.8–8.1 events around Erromango and Tanna Islands to the south (1910, 1913, 1920, and 1950) [*Engdahl and Villasenor*, 2002].

4.6. Seismic Risk

Even if the maximum magnitude is limited to M_w 7.6 in the central section and earthquakes of this magnitude have rarely caused casualties in the Vanuatu archipelago, there is a nonnegligible and growing risk due to the shallow depth of the seismogenic zone beneath the islands and the increase in nonreinforced concrete and cinder block constructions in the region. As for tsunami risk, the probability of tsunamigenic earthquake depends partially on how close the updip limit of plate blocking is to the subduction front, which can best be estimated with geodetic measurements, including offshore [*Ballu et al.*, 2013]. The west coasts of the islands generally rise rapidly above sea level, providing simple escape paths for the population, but the proximity of the coasts to the subduction front (20–40 km) and the rapid deepening of the seafloor offshore may allow little time between an earthquake and the arrival of a tsunami.

4.7. The Shallow Double Seismic Zone

Our local catalog reveals an elongated cloud of earthquakes within the downgoing plate, 20 to 30 km below the subduction interface (red circles in Figure 8). Assuming that the subducting Australian Plate crust is 8 km thick, these earthquakes are located in the subducting plate mantle. They correspond to what has been called the lower layer of the shallow double seismic zone [e.g., *Hacker et al.*, 2003; *Peacock*, 2003].

Two hypotheses have been proposed to explain the existence of shallow lower layer earthquakes: (1) the dehydration of serpentinized mantle at temperatures >600°C [*Peacock*, 2001; *Hacker et al.*, 2003; *Yamasaki*, 2003; *Brudzinski et al.*, 2007] or (2) stresses induced by the flexure of the downgoing slab (dilatational in the crust and compressional in the upper mantle) [*Miyoshi and Obara*, 2011].

The first hypothesis requires the oceanic plate mantle to be hydrated down to 30 km depth, presumably by deep, Moho-crossing, faults before subduction, as suggested by *Ranero et al.* [2005] in western Chile. No such deep faults have been clearly identified on the outer rise of the Australian Plate; however, two events with magnitudes M_w 6.8 and 6.4 occurred in 1992 and 1995 and were located in the outer rise region below the Bougainville seamount (Figure 1). These events have depth lower than 20 km and can suggest that large faults exist, enabling intrusion and circulation of water in the upper mantle. The second hypothesis implies a maximum compressive stress parallel to the convergence direction and subduction interface. Unfortunately, only five of our mechanisms are clearly located in this layer (clusters 13 and 3 and three larger events; Figure 9). The maximum compressive stress axes (*P* axes) of these events are indeed aligned with the convergence direction (~N75°E), but only one of these events has a *P* axis parallel to the subduction interface. Further local focal mechanisms are needed to statistically interpret the origin of the earthquakes in this layer.

5. Conclusion

1. The central part of the Vanuatu arc is characterized by constant and intense low-level seismic activity. More than 30,000 earthquakes were detected and located using 10 months of seismicity in 2008–2009, recorded on a local network covering Santo and north Malekula Islands. The smallest detectable events had $M_L = -0.5$, and 95% of the events had $M_L < 3.1$.
2. We determined a 1-D minimum velocity model from our microseismic catalog. The model is consistent with the 27 ± 4 km thickness calculated by *Coudert et al.* [1984]. Station corrections indicate shallow low-velocity anomalies on the western part of Santo and Malekula, associated with a dense fault network beneath these islands' western mountain chains, and shallow high-velocity anomalies on the eastern part of Santo, associated with the presence of dense compacted limestones.
3. More than half of the earthquake clusters identified through relative relocation have a linear shape. The direction of some of these clusters fall on fault planes indicated by composite focal mechanisms, but their linear shape indicates that they are focused along channels on these planes, which may reveal preexisting elongated geological fragilities. The earthquakes are scattered with time along these channels, with no evidence of propagation along the channel.
4. Focal mechanisms and composite focal mechanisms beneath our network are highly heterogeneous, indicating a complex state of stress in both plates during interseismic loading. This complexity is probably due to the subduction of ridges and seamounts beneath the central Vanuatu arc, creating long-term uplift and both trench-parallel and trench-perpendicular faulting [e.g., *Collot and Fisher*, 1991; *Meffre and Crawford*, 2001]. The correspondence between cluster shapes and focal mechanisms is strong close to the subduction interface and decreases rapidly away, perhaps reflecting the role of strong stresses near this interface in organizing coherent faulting.
5. The 3-D geometry of the subduction interface, defined using our earthquake catalog, a local earthquake catalog from the 2000 M_w 6.9 Santo earthquake and globally determined focal mechanisms, reveals a shallow bulge on the interface in front of the north d'Entrecasteaux ridge and Bougainville seamount. We propose that the buoyancy effect, induced by the subduction of the bathymetric highs, contributes to the upward deformation of the subduction interface and to the long-term uplift observed on Santo and Malekula. Because of this bulge and the proximity of Santo Island to the subduction front, the subduction interface is only 10 km deep beneath the southwest coast of Santo Island, increasing the risk of strong ground motions beneath villages in this region.
6. The downdip limit of the seismogenic zone is ~45 km, which is particularly deep for intraoceanic subduction zones and well below the 27 ± 4 km depth of the upper plate Moho. We propose that this reflects a weak serpentinization of the shallow mantle wedge, which can be explained by a relatively high thermal parameter of the subducting plate increasing the depth at which the subducting crust dehydrates. The subducted bathymetric highs have no apparent effect on this downdip limit.
7. The seismogenic zone is 60–80 km wide in this region. The upper limit of 80 km corresponds to an earthquake magnitude of M_w 7.85 ± 0.4 for complete rupture (considering only the nonstable portion of the interface). Taking into account the probable average width of the zone (~70 km) and apparent seismotectonic barriers

that may limit rupture lengths to 100 km suggests a limit on the order of M_w 7.6 (the largest recorded earthquake in the region was a M_s 7.5 event in 1965). The recurrence cycle for such an event is on the order of 180 years using the currently estimated coupling coefficient and as low as 50 years if long-term coupling is higher. The current seismic gap beneath north Malekula and south Santo is large enough to host a M_w 7.6 earthquake, although the strain accumulated since the 1965 event would only be sufficient to generate such an event if the coupling coefficient is ~1.

8. Our catalog reveals a double seismic zone, whose lower layer is 20 to 30 km below and subparallel to the seismogenic zone. The most likely explanation for this zone is compressional stress associated to the bending of the downgoing plate. A second explanation could be hydrofracturation linked to dehydration of the downgoing plate mantle, but this would require 30 km deep faults on the Australian Plate. More local focal mechanisms are required to distinguish between these two possibilities.

Acknowledgments
We thank the Vanuatu Government and the Vanuatu Geohazards Observatory for their aid and support throughout and beyond the project. The Vanuatu data were collected as part of the ARC-VANUATU program funded by the French National Research Agency (ANR), and the seismometer stations belong to the French national pool of portable seismic instruments SISMOB-RESIF. The earthquake catalog, the velocity model used, and the station coordinates are available online at https://drive.google.com/uc?export=download&id=0BwsPENuZf_J-wUVRla2JUSUJNUkE. Further data can be made available on request to the authors. The authors would like to thank the reviewers for their helpful comments and suggestions that greatly improved the content of this article.

References

Abers, G. (2000), Hydrated subducted crust at 100-250 km depth, *Earth Planet. Sci. Lett.*, *176*(3-4), 323–330, doi:10.1016/S0012-821X(00)00007-8.

Allen, R. (1982), Automatic phase pickers: Their present use and future prospects, *Bull. Seismol. Soc. Am.*, *72*(6), 225–242.

Asanuma, H., M. Ishimoto, R. H. Jones, W. S. Phillips, and H. Niitsuma (2001), A variation of the collapsing method to delineate structures inside a microseismic cloud, *Bull. Seismol. Soc. Am.*, *91*(1), 154–160, doi:10.1785/0120000063.

Baillard, C. (2014), Sismicité et géodynamique dans la zone de subduction du Vanuatu, PhD thesis, Institut de Physique du Globe de Paris, Paris.

Baillard, C., W. C. Crawford, V. Ballu, C. Hibert, and A. Mangeney (2014), An automatic kurtosis-based *P*- and *S*-phase picker designed for local seismic networks, *Bull. Seismol. Soc. Am.*, *104*(1), 394–409, doi:10.1785/0120120347.

Ballu, V., P. Bonnefond, S. Calmant, M.-N. Bouin, B. Pelletier, O. Laurain, W. C. Crawford, C. Baillard, and O. de Viron (2013), Using altimetry and seafloor pressure data to estimate vertical deformation offshore: Vanuatu case study, *Adv. Space Res.*, *51*(8), 1335–1351, doi:10.1016/j.asr.2012.06.009.

Bergeot, N., M. N. Bouin, M. Diament, B. Pelletier, M. Régnier, S. Calmant, and V. Ballu (2009), Horizontal and vertical interseismic velocity fields in the Vanuatu subduction zone from GPS measurements: Evidence for a central Vanuatu locked zone, *J. Geophys. Res.*, *114*, B06405, doi:10.1029/2007JB005249.

Bobet, A., and H. H. Einstein (1998), Fracture coalescence in rock-type materials under uniaxial and biaxial compression, *Int. J. Rock Mech. Min. Sci.*, *35*(7), 863–888, doi:10.1016/S0148-9062(98)00005-9.

Brace, W. F., and E. G. Bombolakis (1963), A note on brittle crack growth in compression, *J. Geophys. Res.*, *68*(12), 3709–3713, doi:10.1029/JZ068i012p03709.

Brudzinski, M. R., C. H. Thurber, B. R. Hacker, and E. R. Engdahl (2007), Global prevalence of double Benioff zones, *Science*, *316*(5830), 1472–1474, doi:10.1126/science.1139204.

Calmant, S., B. Pelletier, P. Lebellegard, M. Bevis, F. W. Taylor, and D. A. Phillips (2003), New insights on the tectonics along the New Hebrides subduction zone based on GPS results, *J. Geophys. Res.*, *108*(B6), 2319, doi:10.1029/2001JB000644.

Castagna, J. P., M. L. Batzle, and R. L. Eastwood (1985), Relationships between compressional-wave and shear-wave velocities in clastic silicate rocks, *Geophysics*, *50*(4), 571–581, doi:10.1190/1.1441933.

Chatelain, J.-L., P. Molnar, R. Prévot, and B. Isacks (1992), Detachment of part of the downgoing slab and uplift of the New Hebrides (Vanuatu) Islands, *Geophys. Res. Lett.*, *19*(14), 1507–1510, doi:10.1029/92GL01389.

Chinn, D. S., and B. L. Isacks (1983), Accurate source depths and focal mechanisms of shallow earthquakes in western South America and in the New Hebrides Island arc, *Tectonics*, *2*(6), 529–563, doi:10.1029/TC002i006p00529.

Cloos, M. (1993), Lithospheric buoyancy and collisional orogenesis: Subduction of oceanic plateaus, continental margins, island arcs, spreading ridges, and seamounts, *Geol. Soc. Am. Bull.*, *105*(6), 715–737, doi:10.1130/0016-7606(1993)105<0715:LBACOS>2.3.CO;2.

Collot, J., J. Daniel, and R. Burne (1985), Recent tectonics associated with the subduction/collision of the d'Entrecasteaux zone in the central New Hebrides, *Tectonophysics*, *112*, 325–356.

Collot, J.-Y., and M. A. Fisher (1991), The collision zone between the north d'Entrecasteaux ridge and the New Hebrides Island arc: 1. SeaBeam morphology and shallow structure, *J. Geophys. Res.*, *96*(B3), 4457, doi:10.1029/90JB01935.

Coudert, E., R. Cardwell, and B. Y. Elisabeth (1984), *P*-wave velocity of the uppermost mantle and crustal thickness in the central Vanuatu Islands (New Hebrides Island arc), *Bull. Seismol. Soc. Am.*, *74*(3), 913–924.

DeMets, C., R. G. Gordon, and D. F. Argus (2010), Geologically current plate motions, *Geophys. J. Int.*, *181*(1), 1–80, doi:10.1111/j.1365-246X.2009.04491.x.

Dessa, J.-X., F. Klingelhoefer, D. Graindorge, C. Andre, H. Permana, M.-A. Gutscher, A. Chauhan, and S. C. Singh (2009), Megathrust earthquakes can nucleate in the forearc mantle: Evidence from the 2004 Sumatra event, *Geology*, *37*(7), 659–662, doi:10.1130/G25653A.1.

Ebel, J. E. (1980), Source processes of the 1965 New Hebrides Islands earthquakes inferred from teleseismic waveforms, *Geophys. J. Int.*, *63*(2), 381–403, doi:10.1111/j.1365-246X.1980.tb02627.x.

Engdahl, E. R., and A. Villasenor (2002), International handbook of earthquake and engineering seismology, in *International Handbook of Earthquake and Engineering Seismology*, vol. 81, edited by W. H. K. Lee et al., pp. 665–690, Elsevier, Amsterdam.

Fehler, M., L. House, and H. Kaieda (1987), Determining planes along which earthquakes occur: Method and application to earthquakes accompanying hydraulic fracturing, *J. Geophys. Res.*, *92*(6), 9407–9414, doi:10.1029/JB092iB09p09407.

Gardner, T. W., D. Verdonck, N. M. Pinter, R. Slingerland, K. P. Furlong, T. F. Bullard, and S. G. Wells (1992), Quaternary uplift astride the aseismic Cocos Ridge, Pacific Coast, Costa Rica, *Geol. Soc. Am. Bull.*, *104*(2), 219–232, doi:10.1130/0016-7606(1992)104<0219:QUATAC>2.3.CO;2.

Gerya, T. V., D. Fossati, C. Cantieni, and D. Seward (2009), Dynamic effects of aseismic ridge subduction: Numerical modelling, *Eur. J. Mineral.*, *21*(3), 649–661, doi:10.1127/0935-1221/2009/0021-1931.

Godano, M., A. Deschamps, S. Lambotte, H. Lyon-Caen, P. Bernard, and F. Pacchiani (2014), Focal mechanisms of earthquake multiplets in the western part of the Corinth Rift (Greece): Influence of the velocity model and constraints on the geometry of the active faults, *Geophys. J. Int.*, doi:10.1093/gji/ggu059.

Hacker, B. R., S. M. Peacock, G. A. Abers, and S. D. Holloway (2003), Subduction factory 2. Are intermediate-depth earthquakes in subducting slabs linked to metamorphic dehydration reactions?, *J. Geophys. Res.*, *108*(B1), 2030, doi:10.1029/2001JB001129.

Hardebeck, J. L. (2003), Using *S/P* amplitude ratios to constrain the focal mechanisms of small earthquakes, *Bull. Seismol. Soc. Am.*, *93*(6), 2434–2444, doi:10.1785/0120020236.

Hardebeck, J. L., and P. M. Shearer (2002), A new method for determining first-motion focal mechanisms, *Bull. Seismol. Soc. Am.*, *92*(6), 2264–2276, doi:10.1785/0120010200.

Hayes, G. P., and D. J. Wald (2009), Developing framework to constrain the geometry of the seismic rupture plane on subduction interfaces a priori—A probabilistic approach, *Geophys. J. Int.*, *176*(3), 951–964, doi:10.1111/j.1365-246X.2008.04035.x.

Hayes, G. P., D. J. Wald, and R. L. Johnson (2012), Slab1.0: A three-dimensional model of global subduction zone geometries, *J. Geophys. Res.*, *117*, B01302, doi:10.1029/2011JB008524.

Heuret, A., S. Lallemand, F. Funiciello, C. Piromallo, and C. Faccenna (2011), Physical characteristics of subduction interface type seismogenic zones revisited, *Geochem. Geophys. Geosyst.*, *12*, Q01004, doi:10.1029/2010GC003230.

Hibert, C., A. Mangeney, G. Grandjean, C. Baillard, D. Rivet, N. M. Shapiro, C. Satriano, A. Maggi, P. Boissier, and V. Ferrazzini (2014), Automated identification, location, and volume estimation of rockfalls at Piton de la Fournaise volcano, *J. Geophys. Res. Earth Surf.*, *119*, 1082–1105, doi:10.1002/2013JF002970.

Husen, S., E. Kissling, E. Flueh, and G. Asch (1999), Accurate hypocentre determination in the seismogenic zone of the subducting Nazca Plate in northern Chile using a combined on-/offshore network, *Geophys. J. Int.*, *138*(3), 687–701, doi:10.1046/j.1365-246x.1999.00893.x.

Hyndman, R. D., M. Yamano, and D. A. Oleskevich (1997), The seismogenic zone of subduction thrust faults, *Isl. Arc*, *6*(3), 244–260, doi:10.1111/j.1440-1738.1997.tb00175.x.

Ide, S. (2013), The proportionality between relative plate velocity and seismicity in subduction zones, *Nat. Geosci.*, *6*(9), 780–784, doi:10.1038/ngeo1901.

Igarashi, T., T. Matsuzawa, and A. Hasegawa (2003), Repeating earthquakes and interplate aseismic slip in the northeastern Japan subduction zone, *J. Geophys. Res.*, *108*(B5), 1–9, doi:10.1029/2002JB001920.

Kennett, B. L. N., and E. R. Engdahl (1991), Traveltimes for global earthquake location and phase identification, *Geophys. J. Int.*, *105*(2), 429–465, doi:10.1111/j.1365-246X.1991.tb06724.x.

Laigle, M., et al. (2013), Seismic structure and activity of the north-central Lesser Antilles subduction zone from an integrated approach: Similarities with the Tohoku forearc, *Tectonophysics*, *603*, 1–20, doi:10.1016/j.tecto.2013.05.043.

Lienert, B. R., and J. Havskov (1995), HYPOCENTER—A computer program for locating earthquakes both locally and globally, *Seismol. Res. Lett.*, *66*(5), 26–36, doi:10.1785/gssrl.66.5.26.

Litchfield, N., S. Ellis, K. Berryman, and A. Nicol (2007), Insights into subduction-related uplift along the Hikurangi Margin, New Zealand, using numerical modeling, *J. Geophys. Res.*, *112*, F02021, doi:10.1029/2006JF000535.

Marthelot, J., J. Chatelain, B. Isacks, R. Cardwell, and E. Coudert (1985), Seismicity and attenuation in the central Vanuatu (New Hebrides) Islands: A new interpretation of the effect of subduction of the d'Entrecasteaux fracture zone, *J. Geophys. Res.*, *90*, 8641–8650, doi:10.1029/JB090iB10p08641.

Maruyama, S., and K. Okamoto (2007), Water transportation from the subducting slab into the mantle transition zone, *Gondwana Res.*, *11*(1-2), 148–165, doi:10.1016/j.gr.2006.06.001.

Meffre, S., and A. J. Crawford (2001), Collision tectonics in the New Hebrides arc (Vanuatu), *Isl. Arc*, *10*(1), 33–50, doi:10.1046/j.1440-1738.2001.00292.x.

Miyoshi, T., and K. Obara (2011), Double seismic zone within the ridge-shaped slab beneath southwest Japan, *Earth, Planets Space*, *62*(12), 949–954, doi:10.5047/eps.2010.11.001.

Nabelek, J. L. (1984), Determination of earthquake source parameters from inversion of body waves, PhD thesis, Massachusetts Institute of Technology, Cambridge.

Pacheco, J. F., L. R. Sykes, and C. H. Scholz (1993), Nature of seismic coupling along simple plate boundaries of the subduction type, *J. Geophys. Res.*, *98*(B8), 14,133–14,159, doi:10.1029/93JB00349.

Peacock, S. M. (2001), Are the lower planes of double seismic zones caused by serpentine dehydration in subducting oceanic mantle?, *Geology*, *29*(4), 299–302, doi:10.1130/0091-7613(2001)029<0299:ATLPOD>2.0.CO;2.

Peacock, S. M. (2003), in *Inside the Subduction Factory*, *Geophys. Monogr. Ser.*, edited by J. Eiler, AGU, Washington, D. C.

Pelletier, B., M. Meschede, T. Chabernaud, P. Roperch, and Z. Xixi (1994), Tectonics of the central New Hebrides arc, North Aoba Basin, in *Proc. ODP*, Sci. Results, vol. 134, edited by H. G. Greene et al., pp. 431–444, College Station, Tex.

Prevot, R., S. W. Roecker, B. L. Isacks, and J. L. Chatelain (1991), Mapping of low *P* wave velocity structures in the subducting plate of the central New Hebrides, southwest Pacific, *J. Geophys. Res.*, *96*(B12), 19,825–19,842, doi:10.1029/91JB01837.

Ranero, C. R., A. Villasenor, J. Phipps Morgan, and W. Weinrebe (2005), Relationship between bend-faulting at trenches and intermediate-depth seismicity, *Geochem. Geophys. Geosyst.*, *6*, Q12002, doi:10.1029/2005GC000997.

Savage, J. C. (1983), A dislocation model of strain accumulation and release at a subduction zone, *J. Geophys. Res.*, *88*(B6), 4984–4996, doi:10.1029/JB088iB06p04984.

Scholz, C. (1998), Earthquakes and friction laws, *Nature*, *391*, 37–42, doi:10.1038/34097.

Scholz, C. H. (2002), *The Mechanics of Earthquakes and Faulting*, Cambridge Univ. Press, Cambridge, U. K.

Shimada, M., A. Cho, and H. Yukutake (1983), Fracture strength of dry silicate rocks at high confining pressures and activity of acoustic emission, *Tectonophysics*, *96*(1-2), 159–172, doi:10.1016/0040-1951(83)90248-2.

Strasser, F. O., M. C. Arango, and J. J. Bommer (2010), Scaling of the source dimensions of interface and intraslab subduction-zone earthquakes with moment magnitude, *Seismol. Res. Lett.*, *81*(6), 941–950, doi:10.1785/gssrl.81.6.941.

Takemura, S., and K. Yoshimoto (2014), Strong seismic wave scattering in the low-velocity anomaly associated with subduction of oceanic plate, *Geophys. J. Int.*, *197*, 1016–1032, doi:10.1093/gji/ggu031.

Taylor, F. W., B. L. Isacks, C. Jouannic, A. L. Bloom, and J. Dubois (1980), Coseismic and Quaternary vertical tectonic movements, Santo and Malekula Islands, New Hebrides Island arc, *J. Geophys. Res.*, *85*(B10), 5367–5381, doi:10.1029/JB085iB10p05367.

Taylor, F. W., R. L. Edwards, G. J. Wasserburg, and C. Frohlich (1990), Seismic recurrence intervals and timing of aseismic subduction inferred from emerged corals and reefs of the central Vanuatu (New Hebrides) frontal arc, *J. Geophys. Res.*, *95*(B1), 393–408, doi:10.1029/JB095iB01p00393.

Taylor, F. W., M. Bevis, B. Schutz, and D. Kuang (1995), Geodetic measurements of convergence at the New Hebrides Island arc indicate arc fragmentation caused by an impinging aseismic ridge, *Geology*, *23*(11), 1011–1014, doi:10.1130/0091-7613(1995)0232.3.CO.

Taylor, F. W., et al. (2005), Rapid forearc uplift and subsidence caused by impinging bathymetric features: Examples from the New Hebrides and Solomon arcs, *Tectonics*, *24*, TC6005, doi:10.1029/2004TC001650.

Tichelaar, B. W., and L. J. Ruff (1993), Depth of seismic coupling along subduction zones, *J. Geophys. Res.*, *98*(B2), 2017–2037, doi:10.1029/92JB02045.

Wai-Ying, C., and H. Kanamori (1978), A mechanical model for plate deformation associated with aseismic ridge subduction in the New Hebrides arc, *Tectonophysics*, *50*(1), 29–40, doi:10.1016/0040-1951(78)90197-X.

Waldhauser, F. (2000), A double-difference earthquake location algorithm: Method and application to the Northern Hayward Fault, California, *Bull. Seismol. Soc. Am.*, *90*(6), 1353–1368, doi:10.1785/0120000006.

Waldhauser, F. (2001), hypoDD—A program to compute double-difference hypocenter locations, *U.S. Geol. Surv. Open File Rep., 01–113,* 25 pp.

Waldhauser, F., and W. L. Ellsworth (2002), Fault structure and mechanics of the Hayward Fault, California, from double-difference earthquake locations, *J. Geophys. Res.*, *107*(B3), 2054, doi:10.1029/2000JB000084.

Yamasaki, T. (2003), Double seismic zone and dehydration embrittlement of the subducting slab, *J. Geophys. Res.*, *108*(B4), 2212, doi:10.1029/2002JB001918.